Published in final edited form as:
J Struct Biol. 2021 October 22; 213(4): 107803. doi:10.1016/j.jsb.2021.107803.

The calcifying interface in a stony coral primary polyp: An interplay between seawater and an extracellular calcifying space

Gal Mor Khalifa[a,b,*], **Shani Levy**[a,b], **Tali Mass**[a,b,*]

Shani Levy: levyshani78@gmail.com

[a]Department of Marine Biology, Leon H. Charney School of Marine Sciences, University of Haifa, Haifa, Israel

[b]Morris Kahn Marine Research Station, The Leon H. Charney School of Marine Sciences, University of Haifa, Haifa, Israel

Abstract

Stony coral exoskeletons build the foundation for the most biologically diverse marine ecosystems on Earth, coral reefs, which face major threats due to many anthropogenic–related stressors. Therefore, understanding coral biomineralization mechanisms is crucial for coral reef management in the coming decades and for using coral skeletons in geochemical studies. This study combines in–vivo imaging with cryo-electron microscopy and cryo–elemental mapping to gain novel insights into the biological microenvironment and the ion pathways that facilitate biomineralization in primary polyps of the stony coral *Stylophora pistillata*. We document increased tissue permeability in the primary polyp and a highly dispersed cell packing in the tissue directly responsible for producing the coral skeleton. This tissue arrangement may facilitate the intimate involvement of seawater at the mineralization site, also documented here. We further observe an extensive filopodial network containing carbon-rich vesicles extruding from some of the calicoblastic cells. Single-cell RNA-Sequencing data interrogation supports these morphological observations by showing higher expression of genes involved in filopodia and vesicle structure and function in the calicoblastic cells. These observations provide a new conceptual framework for resolving the ion pathway from the external seawater to the tissue-mineral interface in stony coral biomineralization processes.

Keywords

Biomineralization; cryo-SEM; cryo-EDS; in-vivo; scRNA-seq; tissue premeability; coral-reef

[*]Corresponding authors at: Morris Kahn Marine Research Station, The Leon H. Charney School of Marine Sciences, University of Haifa, Sdot Yam, Israel. galmor26@gmail.com (G. Mor Khalifa), tmass@univ.haifa.ac.il (T. Mass).

CRediT authorship contribution statement

Gal Mor Khalifa: Conceptualization, Formal analysis, Investigation, Methodology, Validation, Writing – original draft, Writing – review & editing. **Shani Levy:** Formal analysis, Validation, Writing – original draft, Writing – review & editing. **Tali Mass:** Conceptualization, Methodology, Supervision, Writing – original draft, Writing – review & editing.

Declaration of Competing Interest

The authors declare that they have no known competing financial interests or personal relationships that could have appeared to influence the work reported in this paper.

Europe PMC Funders Author Manuscripts

1 Introduction

Stony corals produce calcium carbonate exoskeletons in the form of aragonite that constitute the structural basis of coral reefs ecosystems. On geological time scales, these structures can span thousands of kilometers in shallow tropical and subtropical seas (Darwin, 1845). Coral reefs are vital ecosystems with ecological, evolutionary, and economic importance, yet they are facing major threats today due to multiple anthropogenic stressors. These stressors include global sea–surface warming, ocean acidification, local pollution, overfishing, marine construction, and diving pressure (Ateweberhan et al., 2013; Bozec and Mumby, 2015; Hoegh-Guldberg et al., 2007; Hughes and Connell, 1999; Kennedy et al., 2013). Coral reef risk assessment is a highly complex task because of the multiple stressors involved and the lack of mechanistic understanding of mineral formation at the tissue, cellular and molecular levels. The elemental and isotopic compositions of the aragonitic coral skeletons are used to reconstruct past seawater chemistry and climate. (Adkins et al., 2003; Chalk et al., 2021; Hönisch et al., 2004; Urey et al., 1951; Weber and Woodhead, 1972). Resolving the ion pathway from seawater, through the coral tissue and to the mineralization site, and the biomineralization processes involved is, therefore, essential for better understanding the use of coral skeletons for oceanographic re-constructions, as well as for assessing coral reef fate under current and future climate conditions (Field et al., 2014).

Most scleractinian or stony corals (Anthozoa) form colonies with the basic unit of a polyp. The coral life cycle involves a swimming planula that metamorphoses, settles, and immediately commences rapid calcification to attach firmly to the substrate and form the primary polyp (Vandermeulen, 1975). Polyps have a cylindrical shape with a central mouth surrounded by tentacles used for predation (Fig. 1a. Many stony corals also contain symbiotic dinoflagellates of the family Symbiodiniaceae and feed both by predation and on photosynthetic products supplied by their endosymbionts (LaJeunesse et al., 2018; Martinez et al., 2020; Muscatine, 1973). Coral anatomy includes two body layers, ectoderm and endoderm, separated by a noncellular gelatinous layer called mesoglea. This anatomy repeats itself both in the oral tissue that faces the external seawater and the aboral tissue that faces the exoskeleton (Johnston, 1980). The aboral ectoderm contains calicoblastic cells which are responsible for secreting the mineralized exoskeleton within the space between the skeleton and the tissue also reffered as the sub–skeletal space that is filled with an extracellular medium (ECM) (Allemand et al., 2011; Johnston, 1980; Tambutté et al., 2011b). The skeleton of an individual polyp is composed of radially aligned plates (septa) projecting upwards from the base (Fig. 1a, b, e. Each septum micro-structure includes the first-formed center of calcification (CoC) characterized by a nano-granular texture, while the rest of the septum (its major part in mass) is composed of elongated fibrous micron–sized single crystals arranged in three-dimensional fans (fascicles) around the CoC (Barnes, 1970; Cohen, 2003; Constantz, 1986; Cuif and Dauphin, 1998; Sugiura et al., 2021; Von Euw et al., 2017). The mineral composing the CoC differs from that composing the elongated fibers by structure, elemental and isotopic composition, level of order, and its contained organic matrix (Cuif et al., 2003; Cuif and Dauphin, 2005; 1998; Meibom et al., 2004; Rollion-Bard et al., 2003; Von Euw et al., 2017). The calicoblastic cell layer, the ECM, and the skeletal mineral surface create the microenvironment of coral biomineralization. Detailed

characterization of this microenvironment is essential for resolving the biomineralization strategies in stony corals.

Morphological and spatial characterizations of the tissue-skeleton interface were obtained over the last few decades mainly using conventional scanning electron microscopy (SEM), transmission electron microscopy (TEM) thin sections, and histology (Johnston, 1980; Muscatine et al., 1997; Tambutté et al., 2007). However, these preparation procedures involve chemical fixation, demineralization, staining, dehydration, and plastic or paraffin embedding steps that can cause morphological and chemical alterations of the tissue. Therefore, rapid freezing and freeze-substitution procedures were used to avoid chemical fixation, staining, and demineralization artifacts (Marshall and Wright, 1993). Clode and Marshall were the first to use cryo-fixation followed by low-temperature imaging (i.e., without the need of freeze-substitution) on fully hydrated coral fragments (Clode and Marshall, 2003; 2002a; 2002b) to further achieve preservation of the specimens' original volume and elemental composition (Echlin, 1992). The use of cryo-planing, providing a flat surface of cryo-fixed samples, paved the way for quantification and distribution analysis of dissolved ions in soft tissues and water-based solutions composing the sample using cryo–energy-dispersive x-ray spectroscopy (Cryo-EDS) analysis (Marshall and Wright, 1972; Marshall and Xu, 1998; Marshall, 2017; Mor Khalifa et al., 2018). Cryo–EDS was therefore used to study ion distributions in the coral skeletal-tissue interface (Clode and Marshall, 2002b). Great strides in cryo fixation techniques were made since the pioneering low-temperature observations of Clode and Marshall. This includes high-pressure freezing, in which the necessary heat to be extracted from the specimen is reduced, and thus a fast (milliseconds) cooling procedure allows sample "vitrification", a state in which the water molecules of the sample are kept in a non-crystalline, amorphous solid state, and therefore, as close as possible to natural conditions with respect to sample morphology and elemental distribution (Echlin, 1992; Studer et al., 2008). Another novel in situ measurement of dissolved ion concentration is Ca^{2+} concentrations recently measured in the ECM using microelectrodes (Sevilgen et al., 2019).

A different cutting–edge technique recently applied for the first time in stony corals is single-cell RNA sequencing (scRNA-seq) (Levy et al., 2021), which reveals cellular specialization in stony corals. The new *S. pistillata* cell atlas shows the transcriptional profile of the calicoblastic cells, among other cell types, both in the primary polyp and adult coral (Levy et al., 2021). Thus, it provides insights into the molecular basis of the biomineralization processes carried out by these cells. The recent scRNA-seq analysis of multiple *S. pistillata* life stages also showed that 30% of the primary polyp cells are calicoblasts, while adult colonies are comprised of less than 7% calicoblastic cells (Levy et al., 2021). In addition, the authors reported an increased expression of biomineralization related genes in primary polyps compared with adults (SI Appendix Fig. S1 and (Levy et al., 2021)), supporting the assumption that mineralization activity is more rapid in the primary polyp stage compared with the adult life stage (Gilis et al., 2014; Johnston, 1980; Vandermeulen, 1975). This makes primary polyps good study targets to characterize the mineralization microenvironment and are therefore the subjects of this study.

Here we used cryo-SEM imaging of high–pressure frozen, freeze–fractured or cryo–planed primary polyps to obtain a morphological characterization of the skeleton-tissue interface and to rectify the range of sizes between adjacent calicoblastic cells and between the skeleton and the calicoblastic tissue. We further analyzed the published *S. pistillata* primary polyp cell atlas database (Chang et al., 2019), searching for transcription patterns that correlate with our cryo-SEM morphological analysis. We further obtain a quantitative ion distribution analysis of the ECM fluid using cryo–planing followed by cryo-EDS analysis. Using the described experimental approach, we provide a novel description of the microenvironment in which coral biomineralization occurs and the biomineralization pathway of ions from the seawater through the coral tissue and to the mineralization site.

2 Materials and methods

2.1 Stylophora pistillata primary polyps

S. pistillata larvae were collected from colonies at depths of 8–14 m in the reef adjacent to the Interuniversity Institute of Marine Sciences (IUI), 29°30′06.0″N 34°54′58.3″E, in the Gulf of Aqaba (Israel) under a special permit from the Israeli Natural Parks Authority. Collection was performed using larvae traps made of 160 μm mesh size plankton nets following Neder et al. (Neder et al., 2019). Collected larvae were acclimated overnight under ambient conditions (~25 °C and ~ pH 8.2) in a flow-through outdoor aquarium exposed to natural lighting with fresh seawater filtered to 60 μm. After undergoing metamorphosis, planulae were allowed to settle as primary polyps using seawater volume limitation for a few minutes on a glass bottom dish (for light microscopy) or on a high-pressure freezing aluminum disc, (for cryo–fixation and cryo–SEM imaging). After initial attachment to the substrate, primary polyps were reimmersed in larger seawater volumes. The settled primary polyps commenced mineral deposition and were used for all experiments 4–5 days post-settlement.

2.2 In-vivo fluorescence bead labeling and imaging

In–vivo labeling and imaging was conducted on primary polyps using green fluorescent beads of a 1 μm diameter to test their tissue permeability. Fluorescent bead labeling solution was prepared by diluting 2 μl aqueous suspension of fluorescent yellow-green beads (diameter = 1 μm) (Merck L4655) in 8 ml freshly filtered (0.2 μm) seawater. Primary polyps were incubated in the fluorescent bead labeled seawater solution for 2 hr and imaged on an inverted confocal laser-scanning microscope (Nikon A1R) with both Plan Fluor 10x DIC L and Plan Fluor 40x Oil HN2 objectives. Images were acquired in three channels: green (fluorescence beads excitation: 492 nm emission: 525 ± 50), red (photosymbiont chlorophyll, excitation: 492 nm, emission: 700 ± 75 nm) and laser transmitted image. Pinhole size was 61.3 μm. Time–lapse datasets were obtained using Plan Fluor 10x DIC L objective by acquiring 49 time points in 6 min. Z-stack data sets were acquired using Plan Fluor 40x Oil HN2 objective to cover the entire thickness of the primary polyp tissue in the observed area with 2 μm steps. All images were acquired with the Nikon Nis-Elements software (Nikon Instruments, Melville, NY, United States).

2.3 Cryo-EM techniques

Primary polyps 4–5 days post settlement underwent high-pressure freezing, freeze fracture, cryo-planing and cryo-SEM/EDS imaging. These techniques were performed following Mor Khalifa et al. (Khalifa et al., 2016; Mor Khalifa et al., 2018). In short:

2.4 High-pressure freezing (HPF)

Live 4–5 d old *S. pistillata* primary polyps were immersed in a filtered (0.2 μm) natural seawater solution containing 10 wt% dextran (Fluka) as a cryo-protectant, and immediately high–pressure frozen (HPM10, Bal-Tec AG, Liechtenstein or EM ICE, Leica Microsystems, Vienna, Austria) between two aluminum discs. The mounting procedure took up to 30 sec. Samples for freeze-fracture were frozen between two identical aluminum discs (diameter = 3 mm, thickness = 100 μm) and samples for cryo-planing were frozen inside an aluminum disc of diameter = 3 mm, thickness = 200 μm with a flat aluminum cover.

2.5 Cryo-planing

High-pressure frozen samples were transferred to a cryo-microtome (UC6, Leica Microsystems, Vienna, Austria) and planed at −150 °C in a nitrogen atmosphere to achieve a flat cross-section surface using a diamond blade (Cryotrim 20, DIATOME, Biel, Switzerland). Samples were then vacuumed to 5×10^{-7} mbar, −120 °C (BAF 60, Leica Microsystems, Vienna, Austria) and transferred for cryo-SEM imaging using a vacuum cryo-transfer device (VCT 100, Leica Microsystems, Vienna, Austria). Finally, the samples were loaded into a scanning electron microscope (Ultra 55 S.E.M., Zeiss, Oberkochen, Germany), where they were imaged at – 120 °C.

2.6 Freeze-fracture

High-pressure frozen samples were vacuumed to 5×10^{-7} mbar at – 120 °C and a fracture was conducted at the interface between the two HPF discs containing the sample (BAF 60, Leica Microsystems, Vienna, Austria). One disc containing the exposed cryo-fixed, freeze-fractured primary polyp was transferred for cryo-SEM imaging using a vacuum cryo-transfer device (VCT 100, Leica Microsystems, Vienna, Austria) and loaded into the SEM where it was imaged at – 120 °C.

2.7 Cryo-scanning electron microscopy/energy dispersive spectroscopy (cryo-SEM/EDS) analysis

High-pressure frozen cryo-planed or freeze-fractured *S. pistillata* specimens were loaded into the SEM at –120 °C. Cryo-planed samples were then heated to –105 °C for 3–10 min (etching) to remove adsorbed surface nano-ice crystallites deposited on the sample surface during sample transfer. Freeze fractured samples did not undergo an etching procedure. Samples were then imaged to find loci of interest using an in-lens (in the column) secondary electron (SE) detector and an in-the-column energy selective backscattered electron (EsB) detector using the following microscope conditions: working distance = 2 mm, acceleration voltage = 1.5 kV and aperture = 10 μm. After loci of interest were found and imaged in high resolution using both detectors, cryo–planed samples were transferred using a vacuum cryo-transfer device (VCT 100, Leica Micro–systems, Vienna, Austria) to a freeze-fracture

device (BAF 060; Bal-Tec) for carbon coating (8 nm) before EDS analysis. Samples were transferred back to the electron microscope, and cryo-SEM/EDS analysis was performed using the following microscope conditions: working distance = 7 mm, acceleration voltage = 9 kV, aperture = 30 μm, Cryo-EDS analysis was performed using a Bruker Quantax microanalysis system with an XFlash®6 60 mm detector. Take off angle-35°. Elemental distribution maps and EDS spectra were obtained and analyzed using the Esprite software. Cryo-EDS spectra were collected with 100,000 counts and a comparable measured area (25 ± 2 μm^2) and magnification (x10,000). Background was subtracted and elemental atomic percentages were quantified. Elemental analysis included elemental ratios (ratios between atomic percent of different ions) expressed as the mean ratio ± standard deviation of at least five different measurements. Elemental distribution maps acquisition time was 3 min. Brightness and contrast levels of maps were adjusted using Adobe Photoshop, with identical dynamic range and level adjustments applied to all elemental distribution maps of the same imaged region.

2.8 Image analysis

We used Adobe Photoshop for brightness and contrast level adjustments of cryo-SEM/EDS and in–vivo fluorescence micrographs and manual stitching of high-resolution cryo-SEM micro–graphs to obtain large field-of-view high resolution collage images. We conducted false coloring of SE mode cryo-SEM micrographs to highlight identified loci of interest. Microsoft Excel was used for graphical representation of EDS spectra.

2.9 Single cell RNA-seq data analyses

Gene expression analysis and heatmaps were created from the recently published interactive Shiny application (Chang et al., 2019) “https://sebe-lab.shinyapps.io/Stylophora_cell_atlas/“ based on the *S. pistillata* single cell RNA-Seq (Levy et al., 2021). Gene expression levels as fold-change were normalized by computing a regularized geometric mean within each metacell and dividing this value by the median across metacells.

3 Results

3.1 Morphological characterization of tissue-skeleton interface in primary polyps

Primary polyps were studied 4–5 days after settlement. At this life stage, the primary polyp is adhered to the substrate, tentacles have formed and can be extended by the animal (Fig. 1a, and skeletogenesis is at its early stages in the sessile organism. The basal part of the primary polyp skeleton termed the basal plate, is not yet formed (Fig. 1a. Primary polyps were high-pressure frozen, and the mineral and its adjacent tissue were exposed for imaging, using either freeze-fracture or cryo–planing. The studied areas were roughly in the center between the bottom of the aluminum disk and the septa top to avoid any possible morphological modification of the tissue, which may occur near the bottom part of the polyp due to attachment to a synthetic substrate (Fig. 1b, c, and d. Septa are often not fully developed in the studied primary polyp age and appear non-continuous by conventional light microscopy (Fig. 1e, f). A cryo-SEM energy–selective backscattered electron (EsB) mode image of a high-pressure frozen, freeze-fractured primary polyp reveals two septa with

non-continuous mineral surfaces spread along their long axis (Fig. 1g. Mineral surfaces are detectable with higher contrast (white) than adjacent tissue (grey) using the EsB detector in which the signal is sensitive to atomic number. Studying the freeze-fractured surface of primary polyps, we observed characteristic cells of the oral tissue such as cnidocytes, mucus-forming cells (mucocytes), and host cells containing symbiotic algae (SI Appendix, Fig. S2. We further observe the mineral and the two body layers of the aboral tissue adjacent to it (Fig. 2a. The mineral is indicated by its microcrystalline structure (Fig. 2b, whereas both the aboral endoderm and the aboral ectoderm (i.e., the calicoblastic cell layer) are indicated by their cellular composition in which nuclei and cellular membranes are clearly detected (Fig. 2c. The noncellular mesoglea separating them is identified by its rough surface texture (Fig. 2d, characteristic of a vitrified solution (Mor Khalifa et al., 2018). It is noteworthy that this classical tissue arrangement does not characterize all observed areas. In some of our observed loci cnidocytes were found in close proximity with the mineral (SI Appendix, Fig. S3.

The freeze-fractured surface of a septum (Fig. 3 reveals the microstructure of the first formed mineralization zone, the CoC (Fig. 3c, f-pseudo-orange), characterized by a nano–granulated surface texture composed of tightly packed nano-spheres uniformly sized, 20 ± 3.1 nm (Fig. 3h. The remainder of the septum is composed of elongated fibrous microcrystals arranged in fascicles around the CoC (Fig. 3c, f-pseudo-yellow). The interface between the CoC and the microcrystals layer is better observed in a newly formed septum where the CoC is already completed but the fibrous microcrystals are just starting to form (Fig. 3 d, e, f). The fibrous microcrystals have flat surfaces and are sized up to 1 μm in width and a few microns in length (Fig. 3f, g). The two mineral layers appear to be tightly interwoven.

The calicoblastic cell layer shows various thicknesses, ranging between a monolayer and a layer with a thickness of 4–5 stacked calicoblastic cells. Cell morphology in this layer varies as well (Fig. 4. Some cells of the calicoblastic layer exhibit an elliptical shape (Fig. 4a. Other cells found near the mineral surface typically have an elongated morphology with increasing surface area on the side in contact with the mineral (Fig. 4b. Near mineral corners or sharp edges, calicoblastic cells typically have a cup shape (Fig. 4c. Additionally, many of the observed calicoblastic cells have cellular extensions that span up to several cell diameters and have a typical thickness of hundreds of nm. According to their size and shape, these cellular extensions appear to be a filopodia network and typically occupy the space between the calicoblastic cell layer and the mineral (Fig. 4a, d. These filopodia are enriched with vesicles engulfed by the cell membrane (Fig. 4a, d. High magnification cryo-SEM analysis of a cryo–planed primary polyp reveals the filopodia cross-section and shows that the vast majority of the vesicles are found between two filopodia membranes and thus are intracellular rather than occupying the extracellular space (Fig. 4d. Cryo-EsB images of the same area show that the vesicles do not have an increased electron density, and therefore, presumably, do not contain a solid mineral or dense cation storage (Fig. 4e.

Cryo-SEM/EDS analysis of calicoblastic cells found in close proximity with the septum (Fig. 5 shows that some, but not all, intracellular vesicles are enriched in carbon content

compared with the cell cytoplasm and surrounding tissue. These vesicles can be found both within the calicoblastic cell body (Fig. 5b, c, d and within filopodia (Fig. 5e, f, g).

These morphologicl and elemental analysis observations were consistent across all imaged septa of six freeze-fractured or cryo-planed primary polyps.

3.2 Paracellular spacing in the calicoblastic layer

Moving up the scale from cellular morphology to tissue arrangement of the calicoblastic cell layer, we obtained a large high-resolution overview image of the microenvironment around one septum fracture surface (Fig. 6a, also imaged in Fig. 5 (Fig. 5a-white arrow and Fig. 5e, f, and g). This overview image reveals a highly dispersed packing of calicoblastic cells (Fig. 6a-pseudo burgundy) adjacent to the septum with micrometer-sized spaces between adjacent cell bodies (for example, Fig. 6a-black dashed line = 8.4 μm). The ECM fluid occupying the space between the septum and its neighboring cells is interconnected with these paracellular spaces (Fig. 6a-pseudo blue). Calicoblastic cells become more tightly packed moving away from the septum and into the tissue, where we observed paracellular spaces of tens of nm (Fig. 6a-white arrowhead top right corner). The ECM and paracellular spaces also contain a massive filopodia network (Fig. 6a-pseudo pink) extruding tens of microns away from the calicoblastic cells bodies (Fig. 6a-pseudo burgundy) from which they are derived, towards the septum and containing a large number of vesicles (asterisk) with an average size of 400 ± 100 nm (N = 100).

Moreover, calicoblastic cells of the primary polyps (Fig. 6b-purple) show high expression (compared with other cell types) of genes involved in filopodia network formation and function such as actin, actin-bundling proteins (e.g., fascin), actin-binding proteins (e.g., formins), and Arp2/3 proteins (Fig. 6b. In addition, we found relatively high expression of genes related to vesicular transport, exocytosis, and soluble N-ethylmale-imide-sensitive factor-attachment protein receptors (SNARE) complex, proteins that mediate vesicle fusion such as clathrin, synaptotagmins, and Ras-related proteins (RAPs). This correlates with the large number of vesicles contained within the filopodia network as observed in the cryo-SEM analysis (Fig. 6a-pseudo pink, and Fig. 4d high magnification).

3.3 Tissue permeability

We further studied the overall tissue permeability, i.e., from the external seawater inwards to the primary polyp body by in–vivo labeling with 1 μm diameter fluorescent beads followed by in–vivo imaging. After 2 hr of incubation with seawater solution containing the green-fluorescent beads, the beads were observed to be incorporated inside the primary polyp tissue, as detected in z-stack imaging of the entire primary polyp (Fig. 6c.

3.4 ECM thickness and elemental composition

In–vivo laser-scanning, time-lapse imaging shows a contraction and expansion movement of the aboral tissue near all forming septa of the primary polyp that changes the thickness of the ECM layer facing the septum every few min (Movie S1). The measured ECM thickness at one locus, for example, near the septum, changes from 27 μm to 43 μm within 3 min and back to 18 μm within the next 3 min (Fig. 7a-d. A high-resolution cryo-SEM collage

shows variable ECM layer thicknesses along a septum surface (Fig. 7e ranging from several nm (turquoise arrow-head) up to tens of micrometers (black dashed line-38 μm). Areas with a thick ECM layer bounded by loci of ECM narrowing (asterisks) on either side are referred to as 'ECM pockets' because, together with the septum surface, these areas create semi-delimited ECM spaces.

We further studied the elemental composition of the ECM using quantitative cryo-SEM/EDS analysis of a high-pressure frozen cryo-planed primary polyp (Fig. 8. The mineral is easily differentiated from the ECM and from the soft tissue by its strong Ca signal and slightly increased Na signal (Fig. 8c, f. The major element in both the ECM and the cytoplasm is oxygen (Fig. 8b, d. Increased levels of Na and Cl are observed in the ECM compared with the cytoplasm of calicoblastic cells in which Na and Cl are not detected (Fig. 8b, e and f. We obtained an Cl: Na ratio in the ECM of 1.08 ± 0.05 (Average ratio between atomic percent of the two ions in five different measurements).

4 Discussion

4.1 Morphological characterization of tissue-skeleton interface in primary polyps

Our cryo-SEM observations confirm the mineral microstructure, the aboral tissue layers, and calicoblastic cell morphologies previously documented in stony corals (Cohen, 2003; Johnston, 1980; Marshall and Wright, 1993; Tambutté et al., 2007; Tambutté et al., 2011b) using other imaging techniques. The nonclassical tissue layer arrangement we observed in some locations is also similar to the reduction in tissue layers to two ectodermal layers near a skeletal spine reported in previous studies (Marshall and Wright, 1993; Tambutté et al., 2007). We further show that calicoblastic cells produce elaborate cellular extensions that protrude towards the tissue mineral interface. The large dimensions of these cellular extensions with respect to the calicoblastic cell size (few cell diameter in length and hundreds of nm thickness) and their elaborated shapes suggests that these cell extensions are a filopodial network (Jacinto and Wolpert, 2001; Martín-Blanco and Knust, 2001). We show that the filopodia network contains a multitudinous population of carbon-enriched vesicles. Variable intracellular and extracellular vesicles were previously documented in the calicoblastic ectoderm of several scleractinian corals, some of which are referred to as intracellular fluorescent vesicles assumed to contain an organic material (Marshall and Wright, 1993), secretory vesicles (Le Tissier, 1990; Vandermeulen, 1975), or spherical extracellular material (Johnston, 1980). Our observations support the reports of intracellular vesicles by Clode and Marshall (2002), who also observed the calicoblastic layer in a fully hydrated cryo-fixed coral specimen. Unfortunately, we cannot deduce the vesicle content with the techniques used in this study. Carbon enrichment in these vesicles may be attributed to skeletal organic biomolecules which construct the forming skeleton or to organic molecules used for different physiological processes.

Such extensive vesicle containing filopodia networks as described here were not reported in previous studies of the calicoblast layer of adult scleractinian corals (Ganot et al., 2020; Marshall and Wright, 1993; Tambutté et al., 2007). This may imply that this structure is more characteristic of the primary polyp life stage compared with the adult life stage. The large dimensions of the filopodia network and its multitudinous contained

vesicles documented here in primary polyps are found in agreement with the enrichment of membrane and actin-based cell projections and transport vesicle membrane Gene Ontology (GO) terms associated with primary polyp calicoblastic cells (Levy et al., 2021). It also correlates with our observation of high expression of genes related to filopodia, membrane projection exocytosis, and vesicular transport, in the calicoblastic cells of primary polyps.

The combination of these morphological and molecular results supports an essential role of the observed filopodia network in calicoblastic cell activity, which may be related to the rapid mineralization activity characteristic of the primary polyp life stage. Indeed, an enrichment of the same filopodia-related genes analyzed here was detected in rapid mineralization zones of adult *S. pitillata* colony (branch tip) compared with low mineralization zones (base) of the same colony (Drake et al., 2021), supporting a relation between extensive filopodia procession and rapid mineralization activity.

4.2 Paracellular spacing in the calicoblastic layer

Paracellular spaces were reported (Marshall and Wright, 1993), and their size was estimated in earlier studies on the stony coral calicoblastic layer (Clode and Marshall, 2002a; Le Tissier, 1990; Tambutté et al., 2007; Tambutté et al., 2011a). However, the paracellular spaces reported in this study are significantly larger (reaching several micrometers) than these previous estimations of tens of nm. This highly dispersed cellular arrangement of the calicoblastic layer is intriguing and contradicts the conceptual framework on cell packing in epithelial tissue. One reason why this cellular arrangement is missing from earlier reports is that such loosely attached parts of the tissue found in close proximity with the coral septa may be washed away and eliminated from the sample during post-fixation demineralization and solution exchange procedures involved in sample preparation in some of these earlier studies. We suggest that our observations using high–pressure frozen, fully hydrated samples represent paracellular spacing in the calicoblastic layer as close as possible to natural conditions. Another potential reason for the absence of this tissue arrangement in earlier reports might be related to the fact that it is more characteristic of the primary polyps than of the adult life stage, which was mainly used in previous studies.

We also report that cellular packing can vary between dispersed and tight arrangements at different locations within the same coral specimen. It is yet unclear whether the observed differential arrangement is actively controlled. One function of a dispersed cellular arrangement may be to change tissue permeability spatially and temporally. Corals were shown to control their overall body permeability and to modify it in response to external stressors such as osmotic pressure and temperature change (Venn et al., 2020). It is, therefore, reasonable to assume that they can also locally modify their tissue permeability across different parts of the forming skeleton according to their needs.

4.3 Tissue permeability

Indications for seawater paracellular pathways were reported in stony coral tissue using in-vivo labeling (Ganot et al., 2020; Ohno et al., 2017; Tambutté et al., 2011a; Venn et al., 2020). Tissue permeability tests performed on adult *S. pistillata* microcolonies showed that molecules and particles of sizes between 13 Å-20 nm diffuse from the external seawater into

the coral tissue via the paracellular pathway. Therefore, this size was considered the size of the intercellular junctions connecting one cell to another, i.e., the coral 'septate junctions' (Ganot et al., 2015; Tambutté et al., 2011a; Tambutté et al., 2007). In this study, however, we observe significantly higher permeability in the oral epithelial tissue of primary polyps of the same coral species, with particles of 1 μm size passing through their oral epithelial tissue, a size that cannot be attributed to a septate junction (Ganot et al., 2015). Nevertheless, for septate junction size to impose whole tissue permeability, an assumption must be made that all adjacent cells are attached to one another via septate junctions. The dispersed cell packing of the calicoblastic layer with paracellular spaces of a few micrometer sizes, documented here, challenges this basic assumption. We infer that while some calicoblastic cells are attached to all neighboring cells via septate junctions, others are bathed within the ECM, separated by a few microns from some of their adjacent cells in the primary polyp. These observations suggest that septate junction dimensions do not solely define tissue permeability. We note that our fluorescence imaging analysis is used here to study the permeability of the oral epithelium, and we cannot infer the specific body layer (or layers) to which the 1 μm fluorescent beads were incorporated using this technique alone.

4.4 ECM thickness and elemental composition

The ECM is the site where aragonite microcrystals comprising the coral skeleton crystalize and grow (Ohno et al., 2017; Tambutté et al., 2011b). It is primarily documented as a thin noncellular fluid or gelatinous layer with a thickness of nanometers to 1 μm, filling the space between the mineral and the calicoblastic tissue (Clode and Marshall, 2002a; Cohen, 2003; Tambutté et al., 2007; Tambutté et al., 2011b). Recent studies show growing evidence of areas where calicoblastic tissue is locally lifted away from the mineral, creating semi-delimited ECM spaces referred to as 'ECM pockets' (Ohno et al., 2017), as previously hypothesized (Barnes, 1970; Cohen, 2003). The cryo-fixation technique used here preserves the ECM fluid's original volume and allows us to measure the exact ECM thickness at different locations along the primary polyp septum. The ECM thickness observed in some ECM pockets was significantly larger (by an order of magnitude) than previous ECM thickness estimations (Johnston, 1980; Le Tissier, 1990; Tambutté et al., 2007; Tambutté et al., 2011b). We further show that ECM thickness is highly variable along a single septum. Our in-vivo observations reveal contraction movements that modify the ECM layer thickness simultaneously along the forming septa of the entire primary polyp, similar to contraction and expansion movement documented in *A. digitifera* primary polyps (Ohno et al., 2017).

The observation that ECM pockets can reach tens of microns in thickness also helps to explain another recent observation of primary cilia in some calicoblastic cells of *S. pistillata* micro-colonies (Tambutté et al., 2020). Primary cilia are morphologically different from filopodia by their shorter length and straight stalk-like morphology, and they are restricted to one primary cilium per cell. Primary cilia act as mechanosensors that translate extracellular stimulations from the external micro-environment to intracellular signals in different organisms (Alaiwi et al., 2009), and in the case of corals, they are thought to transfer signals from the ECM to the calicoblastic cells (Tambutté et al., 2020). One question raised by those authors is whether the cilia have enough space in the ECM to stretch and bend, considering their length of 1–2 μm. Our observations of the range of ECM thicknesses

show that they certainly do. Therefore, it is possible that primary cilia play a role in sensing and controlling ECM fluid flow inside ECM pockets.

The cryo-EDS analysis of the ECM implies that it contains incorporated external seawater. This is due to the fact that the major element in the ECM cryo-EDS spectrum is oxygen, implying the ECM is mainly a water-based solution (Marshall and Xu, 1998; Mor Khalifa et al., 2018). In addition, the Cl^- to Na^+ ratios in the ECM are similar to those ratios in seawater, i.e., 1.13 (Pilson, 2012), and different from the cellular Cl^- to Na^+ ratio, which is 0.8 or lower (O. S. Andersen, 2013). This is unlikely to result from a controlled active cellular transport of Cl^- and Na^+ ions to the ECM. Unfortunately, we could not detect other major seawater ions such as Mg^{2+}, SO_4^{2-}, Ca^{2+}, and K^+ in the ECM as their natural concentrations in seawater are below the detection limit of the specific cryo-EDS protocol used in this study (Mor Khalifa et al., 2018). The cryo-EDS spectrum of the calicoblastic cytoplasm does not show detectable Na and Cl peaks. This is expected since cellular concentrations of Na (12 mM), and Cl (10 mM) (O. S. Andersen, 2013) are below the detection limits of this protocol which are 25–50 mM and 50–73 mM, respectively (Mor Khalifa et al., 2018). Some differences between the preparation and acquisition conditions used in this protocol and other cryo-EDS protocols reported in the literature (Clode and Marshall, 2002b; Marshall, 2017) may result in different detection limits reported. These observations provide a further indication for the incorporation of the external seawater into the ECM suggested in previous studies using different experimental techniques (Clode and Marshall, 2004; 2003; Clode and Marshall, 2002a; Gagnon et al., 2012; Hönisch et al., 2012; Ohno et al., 2017).

5 Conclusions

We used a combined structural, chemical, live imaging, and molecular approach to elucidate intriguing tissue arrangements in primary polyps of the stony coral *S. pistillata*. These include high tissue permeability, an extensive filapodia network, large paracellular spaces in the calicoblastic layer, large ECM pockets with incorporated seawater content, and intensive tissue contraction and expansion activity. When integrated, these observations may imply rapid delivery of external seawater to the mineralization site, possibly as part of the mineralization strategy. We used the primary polyp life stage to study biomineralization pathways because it is characterized by rapid mineralization activity, and therefore mineralization mechanisms may appear more pronounced in this life stage. Indeed, the dimensions and manifestation intensity of the tissue arrangments described here are strikingly more prominent in the primary polyp than its adult counterpart.

Possible similar manifestation of these tissue arrangements may occur in loci of rapid mineralization within adult colonies, similarly to the enriched expression of filopodia-related genes observed both here on primary polyps and in rapid mineralization zones of the adult colony of the same species (Drake et al., 2021).

Previous morphological and mineralogical studies of the mineral formed in primary polyps of similar age as studied here suggested a “less controlled” mineralization process involving the direct entering of seawater between the tissue and the substrate with the newly deposited

skeleton (Gilis et al., 2014). Our observations were conducted on the middle part of the septa, i.e., far from possible interference of the substrate, and implicate a controlled tissue arrangement that is actively modified along the primary polyp body.

A possible role for incorporating external seawater into the ECM is to use dissolved ions and especially Ca^{2+} ions directly from seawater for biomineralization. One model discussed in the literature is ion-by-ion crystallization from a saturated solution of the aragonite microcrystals composing the coral skeleton, where the ECM fluid functions as the mother solution for mineralization (Erez et al., 2011). Stable isotope incorporation studies support the ion-by-ion strategy and suggest that the major part of Ca^{2+} ions used for coral biomineralization is delivered as dissolved Ca^{2+} ions in seawater which is incorporated into the ECM, rather than active Ca^{2+} pumping (Gagnon et al., 2012). This strategy requires cycling large volumes of modified seawater, i.e., the mother solution for mineralization, in the organism's body. A missing link in this model is the ratio between the volume of the ECM and the surface area of the septum mineral, i.e., the ECM thickness considering a simplified box shape of the ECM. The ion-by-ion mineralization model predicts an ECM thickness of tens of μm, l (Gagnon et al., 2021, 2012) and therefore observations of the current study support the feasibility of this mode. However, our observations of high spatiotemporal variations of the ECM thickness impose more complexity on the calculations of seawater turn–over rates than using a simplified box model with a constant ECM thickness. Spatial variability of the ECM thickness along the septum may also suggest active tuning of the ECM size and shape according to mineralization needs, such as the creation of semi-delimited ECM pockets. This is also found in agreement with previous observations that coral mineralization is non-continuous across the skeleton but is somewhat patchy on a spatial scale of tens of microns (Gagnon et al., 2012; Houlbrèque et al., 2009). The changing of tissue permeability may be a way to increase seawater and ion supply to the mineralization site during periods of rapid mineralization activity. Additionally, increasing calicoblastic cell surface area in contact with seawater, facilitated by the large paracellular spaces, may thus increase the absorption of ions from the seawater into the cells. However, any relation between locally increased tissue permeability and the mineralization activity has yet to be demonstrated.

While some evidence supports an ion-by-ion crystallization from a saturated solution strategy exploited in stony corals skeletogenesis, other observations support an alternative crystallization strategy involving intracellular Ca^{2+} ion accumulation (Clode and Marshall, 2004) and crystallization via an amorphous calcium carbonate (ACC) precursor phase (Akiva et al., 2018; Mass et al., 2017). In this study, we did not observe any dense Ca^{2+} storage compartments in the calicoblastic cell layer, the ECM, or in the other coral tissue layers, despite Ca^{2+} concentrations in an ACC phase, typically in the molar range (Kahil et al., 2020), that are well within the detection limit of the cryo-EDS technique. However, this negative observation does not rule out the existence of such phases in other parts of the primary polyp body, in sizes smaller than our resolution limits (few nm) or in times points or life stages other than that of the primary polyps studied here. Mineralization via an ACC precursor may also be more pronounced in the CoCs that compose the coral skeleton's minor part (by mass). The mineral composing the CoC is enriched in Mg (Meibom et al., 2004), which was shown to stabilize transient ACC precursor phases

used in biomineralization processes (Raz et al., 2003). The CoC is further characterized with a nano-granulated surface texture typical of biominerals formed via an ACC precursor (Gal et al., 2014). In contrast, the elongated microcrystals composing the major part of the skeleton mass are characterized by micron-sized flat facets as observed here in the newly formed septum and in previous studies (Sugiura et al., 2021), and may be more characteristic of minerals formed from a saturated solution. The literature has also proposed a bi-model combining both mineralization strategies via an ACC precursor and ion-by-ion mineralization from a saturated solution (Sun et al., 2020).

Regardless of the function that tissue permeability modification plays in stony corals, the fact that primary polyps have higher tissue permeability than adult coral colonies may make them more vulnerable to local contamination such as microplastics, sewage pollution, and sediment suspension. Their rapid internalization of external seawater into their mineralization site may also make these newly recruited corals more vulnerable than adult corals to ocean acidification. These observations should, therefore, be considered in risk assessment and coral reef management.

Supplementary Material

Refer to Web version on PubMed Central for supplementary material.

Acknowledgments

We would like to thank Dr. Neta Varsano for the illustration in Fig. 1a-d; Dr. Eyal Shimoni from the Electron microscopy unit, Weizmann Institute of Sciences, Israel and Dr. Assaf Gal from the Weizmann Institute of Science, Israel for their help with the cryo-SEM/EDS analysis; Dr. Boris Shklyar at the Bioimaging unit, Faculty of natural sciences, University of Haifa, Israel for his guidance and technical support with the in-vivo imaging; Dr. Jeana Drake for her advice and proofreading and to Maayan Neder, Itay Kolsky and Federica Scucchia for their help with sample collection and to Rahel Prado for primary polyp image in the graphical abstract.

Funding

This work has received funding from the European Research Council under the European Union's Horizon 2020 research and innovation programme (grant agreement No 755876).

Data availability

The authors declare that all the data supporting the findings of this study are available within the article and its Supplementary Information files. Extra data are available from the corresponding author upon request.

References

Adkins JF, Boyle EA, Curry WB, Lutringer A. Stable isotopes in deep-sea corals and a new mechanism for "vital effects". Geochim Cosmochim Acta. 2003; 67 :1129–1143.

Akiva A, Neder M, Kahil K, Gavriel R, Pinkas I, Goobes G, Mass T. Minerals in the pre-settled coral Stylophora pistillata crystallize via protein and ion changes. Nat Commun. 2018; 9 :1–9. [PubMed: 29317637]

Alaiwi WAA, Lo ST, Nauli SM. Primary cilia: highly sophisticated biological sensors. Sensors. 2009; 9 :7003–7020. [PubMed: 22423203]

Allemand, D, Tambutté, E, Zoccola, D, Tambutté, S. Coral Reefs: An Ecosystem in Transition. Springer; Netherlands: 2011. 119–150.

Ateweberhan M, Feary DA, Keshavmurthy S, Chen A, Schleyer MH, Sheppard CRC. Climate change impacts on coral reefs: Synergies with local effects, possibilities for acclimation, and management implications. Mar Pollut Bull. 2013; 74 :526–539. [PubMed: 23816307]

Barnes DJ. Coral skeletons: an explanation of their growth and structure. Science. 1970; 170 :1305–1308. [PubMed: 17829430]

Bozec YM, Mumby PJ. Synergistic impacts of global warming on the resilience of coral reefs. Philos Trans R Soc B Biol Sci. 2015; 370 :1–9.

Chalk TB, Standish CD, Angelo CD, Castillo KD, Milton JA, Foster GL. Mapping coral calcification strategies from in situ boron isotope and trace element measurements of the tropical coral Siderastrea siderea. Sci Rep. 2021 :1–14. [PubMed: 33414495]

Chang W, Cheng J, Allaire JJ, Xie Y, McPherson J. shiny: Web Application Framework for R. R Packag version 1.4.0. 2019

Clode PL, Marshall AT. Calcium localisation by X-ray microanalysis and fluorescence microscopy in larvae of zooxanthellate and azooxanthellate corals. Tissue Cell. 2004; 36 :379–390. [PubMed: 15533453]

Clode PL, Marshall AT. Calcium associated with a fibrillar organic matrix in the scleractinian coral Galaxea fascicularis. Protoplasma. 2003; 220 :153–161. [PubMed: 12664279]

Clode PL, Marshall AT. Low temperature FESEM of the calcifying interface of a scleractinian coral. Tissue Cell. 2002a; 34 :187–198. [PubMed: 12182812]

Clode PL, Marshall AT. Low temperature X-ray microanalysis of calcium in a scleractinian coral:evidence of active transport mechanisms. J Exp Biol. 2002b; 205 :3543–3552. [PubMed: 12364407]

Cohen AL. Geochemical perspectives on coral mineralization. Rev Mineral Geochem. 2003; 54 :151–187.

Constantz BR. Coral Skeleton Construction: A Physiochemically Dominated Process. 1986; 1 :152–157.

Cuif J-P, Dauphin Y. The two-step mode of growth in the scleractinian coral skeletons from the micrometre to the overall scale. J Struct Biol. 2005; 150 :319–331. [PubMed: 15890280]

Cuif J-P, Dauphin Y. Microstructural and physico-chemical characterization of ‘centers of calcification’ in septa of some Recent scleractinian corals. Paläontologische Zeitschrift. 1998; 72 :257–269.

Cuif J-P, Dauphin Y, Doucet J, Salome M, Susini J. XANES mapping of organic sulfate in three scleractinian coral skeletons. 2003

Darwin C. The structure and distribution of coral reefs; being the first part of the geology of the voyage of the beagle under the command of Capt. Fitzroy, R.N. during the years 1832 to 1836. Quarterly Journal of the Geological Society of London. 1845

Drake JL, Malik A, Popovits Y, Yosef O, Shemesh E, Stolarski J, Tchernov D, Sher D, Mass T. Physiological and transcriptomic variability indicative of differences in key functions within a single coral colony. Front Mar Sci. 2021; 768

Echlin, P. Low-Temperature Microscopy and Analysis. Echlin, P, editor. Springer; US: 1992. 491–498.

Erez, J, Reynaud, S, Silverman, J, Schneider, K, Allemand, D. Coral Reefs: An Ecosystem in Transition. Springer; Netherlands: 2011. 151–176.

Field, CB, Barros, VR, Dokken, DJ, Mach, KJ, Mastrandrea, MD, Bilir, TE, Chatterjee, M, Ebi, KL, Estrada, YO, Genova, RC, Girma, B. , et al. Climate change 2014 impacts, adaptation and vulnerability: Part A: global and sectoral aspects. Intergovernmental panel on climate change; 2014.

Gagnon AC, Adkins JF, Erez J. Seawater transport during coral biomineralization. Earth Planet Sci Lett. 2012; 329–330 :150–161.

Gagnon AC, Gothmann AM, Branson O, Rae JWBB, Stewart JA. Controls on boron isotopes in a cold-water coral and the cost of resilience to ocean acidification. Earth Planet Sci Lett. 2021; 554 116662

Gal A, Kahil K, Vidavsky N, Devol RT, Gilbert PUPA, Fratzl P, Weiner S, Addadi L. Particle accretion mechanism underlies biological crystal growth from an amorphous precursor phase. Adv Funct Mater. 2014; 24 :5420–5426.

Ganot P, Tambutté E, Caminiti-Segonds N, Toullec G, Allemand D, Tambutté S. Ubiquitous macropinocytosis in anthozoans. Elife. 2020; 9 :1–25.

Ganot P, Zoccola D, Tambutté E, Voolstra CR, Aranda M, Allemand D, Tambutté S. Structural molecular components of septate junctions in cnidarians point to the origin of epithelial junctions in Eukaryotes. Mol Biol Evol. 2015; 32 :44–62. [PubMed: 25246700]

Gilis AM, Meibom A, Domart-Coulon I, Grauby O, Jarosław S, Baronnet A. Biomineralization in newly settled recruits of the scleractinian coral pocillopora damicornis. Morphology. 2014 :1–17.

Hoegh-Guldberg O, Mumby PJ, Hooten AJ, Steneck RS, Greenfield P, Gomez E, Harvell CD, Sale PF, Edwards AJ, Caldeira K, Knowlton N, et al. Coral reefs under rapid climate change and ocean acidification. Science. 2007; 318 :1737–1742. [PubMed: 18079392]

Hönisch B, Hemming NG, Grottoli AG, Amat A, Hanson GN, Bijma J. Assessing scleractinian corals as recorders for paleo-pH: empirical calibration and vital effects. Geochim Cosmochim Acta. 2004; 68 :3675–3685.

Hönisch B, Ridgwell A, Schmidt DN, Thomas E, Gibbs SJ, Sluijs A, Zeebe R, Kump L, Martindale RC, Greene SE, Kiessling W, et al. The geological record of ocean acidification. Science. 2012; 335 :1058–1063. [PubMed: 22383840]

Houlbrèque F, Meibom A, Cuif JP, Stolarski J, Marrocchi Y, Ferrier-Pagès C, Domart-Coulon I, Dunbar RB. Strontium-86 labeling experiments show spatially heterogeneous skeletal formation in the scleractinian coral Porites porites. Geophys Res Lett. 2009; 36

Hughes TP, Connell JH. Multiple stressors on coral reefs: a long-term perspective. Limnol Oceanogr. 1999; 44 :932–940.

Jacinto A, Wolpert L. Quick guide Filopodia. Curr Biol. 2001; 11 R634 [PubMed: 11525752]

Johnston, IS. International Review of Cytology. Academic Press; 1980. 171–214.

Kahil K, Varsano N, Sorrentino A, Pereiro E, Rez P, Weiner S, Addadi L. Cellular pathways of calcium transport and concentration towards mineral formation in sea urchin larvae. Proc Natl Acad Sci USA. 2020; 117 :30957–30965. [PubMed: 33229583]

Kennedy EV, Perry CT, Halloran PR, Iglesias-Prieto R, Schönberg CHL, Wisshak M, Form AU, Carricart-Ganivet JP, Fine M, Eakin CM, Mumby PJ. Avoiding coral reef functional collapse requires local and global action. Curr Biol. 2013; 23 :912–918. [PubMed: 23664976]

Khalifa GM, Kirchenbuechler D, Koifman N, Kleinerman O, Talmon Y, Elbaum M, Addadi L, Weiner S, Erez J. Biomineralization pathways in a foraminifer revealed using a novel correlative cryo-fluorescence-SEM-EDS technique. J Struct Biol. 2016; 196 :155–163. [PubMed: 26828113]

LaJeunesse TC, Parkinson JE, Gabrielson PW, Jeong HJ, Reimer JD, Voolstra CR, Santos SR. Systematic revision of symbiodiniaceae highlights the antiquity and diversity of coral endosymbionts. Curr Biol. 2018; 28 :2570–2580. e6 [PubMed: 30100341]

Le Tissier MDA. The ultrastructure of the skeleton and skeletogenic tissues of the temperate coral caryophyllia smithii. J Mar Biol Assoc United Kingdom. 1990; 70 :295–310.

Levy S, Elek A, Grau-Bové X, Mené ndez-Bravo S, Iglesias M, Tanay A, Mass T, Sebe-Pedro A. A stony coral cell atlas illuminates the molecular and cellular basis of coral symbiosis, calcification, and immunity. Cell. 2021; 184 :1–15. [PubMed: 33417857]

Marshall AT, Wright A. Detection of diffusible ions in insect osmoregulatory systems by electron probe X-ray microanalysis using scanning electron microscopy and a cryoscopic technique. Micron. 1972; 1969 (4) :31–45.

Marshall AT, Wright OP. Confocal laser scanning light microscopy of the extra-thecal epithelia of undecalcified scleractinian corals Cell Tissue Res. 1993; 272 (3) :533–543.

Marshall AT, Xu W. Quantitative elemental X-ray imaging of frozen-hydrated biological samples. J Microsc. 1998; 190 :305–316. [PubMed: 9674156]

Marshall TA. Quantitative x-ray microanalysis of model biological samples in the SEM using remote standards and the XPP analytical model. J Microsc. 2017; 266 :231–238. [PubMed: 28181671]

Martín-Blanco E, Knust E. Epithelial morphogenesis: filopodia at work. Curr Biol. 2001; 11 :28–31.

Martinez S, Kolodny Y, Shemesh E, Scucchia F, Nevo R, Levin-Zaidman S, Paltiel Y, Keren N, Tchernov D, Mass T. Energy sources of the depth-generalist mixotrophic coral Stylophora pistillata. Front Mar Sci. 2020; 7 :988. [PubMed: 33409285]

Mass T, Giuffre AJ, Sun CY, Stifler CA, Frazier MJ, Neder M, Tamura N, Stan CV, Marcus MA, Gilbert PUPA. Amorphous calcium carbonate particles form coral skeletons. Proc Natl Acad Sci USA. 2017; 114 :E7670–E7678. [PubMed: 28847944]

Meibom A, Cuif J-P, Hillion F, Constantz B, Juillet-Leclerc A, Dauphin Y, Watanabe T, Dunbar R, Constantz BR, Dunbar RB. Distribution of magnesium in coral skeleton. Geophys Res Lett. 2004; 31

Mor Khalifa G, Kahil K, Erez J, Kaplan Ashiri I, Shimoni E, Pinkas I, Addadi L, Weiner S. Characterization of unusual MgCa particles involved in the formation of foraminifera shells using a novel quantitative cryo SEM/EDS protocol. Acta Biomater. 2018; 77 :342–351. [PubMed: 30026104]

Muscatine, L. 4 - NUTRITION OF CORALS. Jones, OA, Endean, RBT-B, CR, G, editors. Academic Press; 1973. 77–115.

Muscatine L, Tambutté E, Allemand D. Morphology of coral desmocytes, cells that anchor the calicoblastic epithelium to the skeleton. Coral Reefs. 1997; 16 :205–213.

Neder M, Laissue PP, Akiva A, Akkaynak D, Albéric M, Spaeker O, Politi Y, Pinkas I, Mass T. Mineral formation in the primary polyps of pocilloporoid corals. Acta Biomater. 2019; 96 :631–645. [PubMed: 31302296]

Andersen, OS. Encyclopedia of Metalloproteins. Kretsinger, RH, Uversky, VN, Permyakov, EA, editors. Springer-Verlag; New York: 2013. 580–587.

Ohno Y, Iguchi A, Shinzato C, Gushi M, Inoue M, Suzuki A, Sakai K, Nakamura T. Calcification process dynamics in coral primary polyps as observed using a calcein incubation method. Biochem Biophys Reports. 2017; 9 :289–294.

Pilson, MEQ. An Introduction to the Chemistry of the Sea. Pilson, MEQ, editor. Vol. 67. Cambridge University Press; 2012.

Raz S, Hamilton PC, Wilt FH, Weiner S, Addadi L. The transient phase of amorphous calcium carbonate in sea urchin larval spicules: the involvement of proteins and magnesium ions in its formation and stabilization. Adv Funct Mater. 2003; 13 :480–486.

Rollion-Bard C, Blamart AD, Cuif J-P, Juillet-Leclerc A, Blamart D, Cuif J-P, Juillet-Leclerc A. Microanalysis of C and O isotopes of azooxanthellate and zooxanthellate corals by ion microprobe. Coral Reefs. 2003; 22 (4) :405–415.

Sevilgen DS, Venn AA, Hu MY, Tambutté E, De Beer D, Planas-Bielsa V, Tambutté S. Full in vivo characterization of carbonate chemistry at the site of calcification in corals. Sci Adv. 2019; 5 eaau7447 [PubMed: 30746460]

Studer D, Humbel BM, Chiquet M. Electron microscopy of high pressure frozen samples: bridging the gap between cellular ultrastructure and atomic resolution. Histochem Cell Biol. 2008; 130 :877–889. [PubMed: 18795316]

Sugiura M, Yasumoto K, Iijima M, Oaki Y, Imai H. Morphological study of fibrous aragonite in the skeletal framework of a stony coral. CrystEngComm. 2021; 23 :3693–3700.

Sun CY, Stifler CA, Chopdekar RV, Schmidt CA, Parida G, Schoeppler V, Fordyce BI, Brau JH, Mass T, Tambutté S, Gilbert PUPA. From particle attachment to space-filling coral skeletons. Proc Natl Acad Sci USA. 2020; 117 :30159–30170. [PubMed: 33188087]

Tambutté E, Allemand D, Zoccola D, Meibom A, Lotto S, Caminiti N, Tambutté S. Observations of the tissue-skeleton interface in the scleractinian coral Stylophora pistillata. Coral Reefs. 2007; 26 :517–529.

Tambutté E, Ganot P, Venn AA, Tambutté S. A role for primary cilia in coral calcification? Cell Tissue Res. 2020; 383 :1093–1102. [PubMed: 33330957]

Tambutté E, Tambutté S, Segonds N, Zoccola D, Venn A, Erez J, Allemand D. Calcein labelling and electrophysiology: insights on coral tissue permeability and calcification. Proc R Soc B Biol Sci. 2011a; 279 :19–27.

Tambutté S, Holcomb M, Ferrier-Pagés C, Reynaud S, Tambutté É, Zoccola D, Allemand D. Coral biomineralization: from the gene to the environment. J Exp Mar Bio Ecol. 2011b; 408 :58–78.

Urey HC, Lowenstam HA, Epstein S, McKinney CR. Measurement of paleotemperatures and temperatures of the upper cretaceous of England, Denmark and the southeastern United state. GSA Bull. 1951; 62 :399–416.

Vandermeulen JH. Studies on reef corals. III. Fine structural changes of calicoblast cells in Pocillopora damicornis during settling and calcification. Mar Biol. 1975; 31 :69–77.

Venn AA, Bernardet C, Chabenat A, Tambutté E, Tambutté S. Paracellular transport to the coral calcifying medium: effects of environmental parameters. J Exp Biol. 2020; 223

Von Euw S, Zhang Q, Manichev V, Murali N, Gross J, Feldman LC, Gustafsson T, Flach C, Mendelsohn R, Falkowski PG. Biological control of aragonite formation in stony corals. Science. 2017; 356 :933–938. [PubMed: 28572387]

Weber JN, Woodhead PMJ. Temperature dependence of oxygen-18 concentration in reef coral carbonates. J Geophys Res. 1972; 77 :463–473.

Europe PMC Funders Author Manuscripts

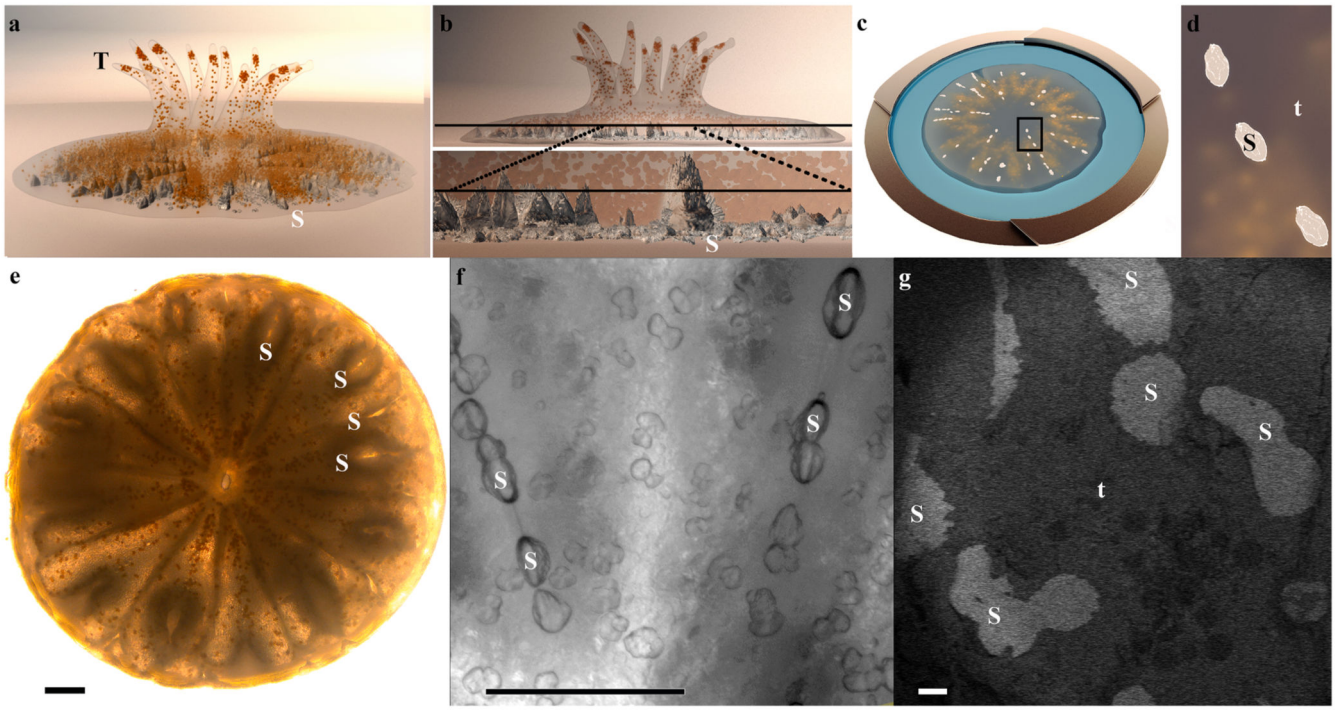

Fig. 1. A primary polyp and its forming mineralized septa.

(a) Illustration of a few days old primary polyp. Endosymbionts are orange, and mineral is grey. (b) Upper panel: An illustration of the same polyp as in (a) in a side view, with internal plane revealed by cryo-planing or freeze–fracture marked with a black line. Bottom panel: Magnification of this plane crossing two septa. (c) Illustration of high-pressure frozen, cryo–planed primary polyp (top view) vitrified in natural seawater (blue) inside a high-pressure freezing disc (gold). (d) Magnification of the area marked with black rectangle in (c). (e) Light microscopy image of a primary polyp. (f) Higher magnification wide-field microscope image of two forming septa. (g) Cryo-SEM (EsB mode) micrograph of freeze fractured primary polyp showing the non-continuous fracture surface of two forming septa. Septa mineral surface appears white, and coral tissue surface appears grey. **T**-tentacles, **S**-septum mineral, **t**-tissue. Scale bars: e, f, – 100 μm, g – 20 μm.

Europe PMC Funders Author Manuscripts

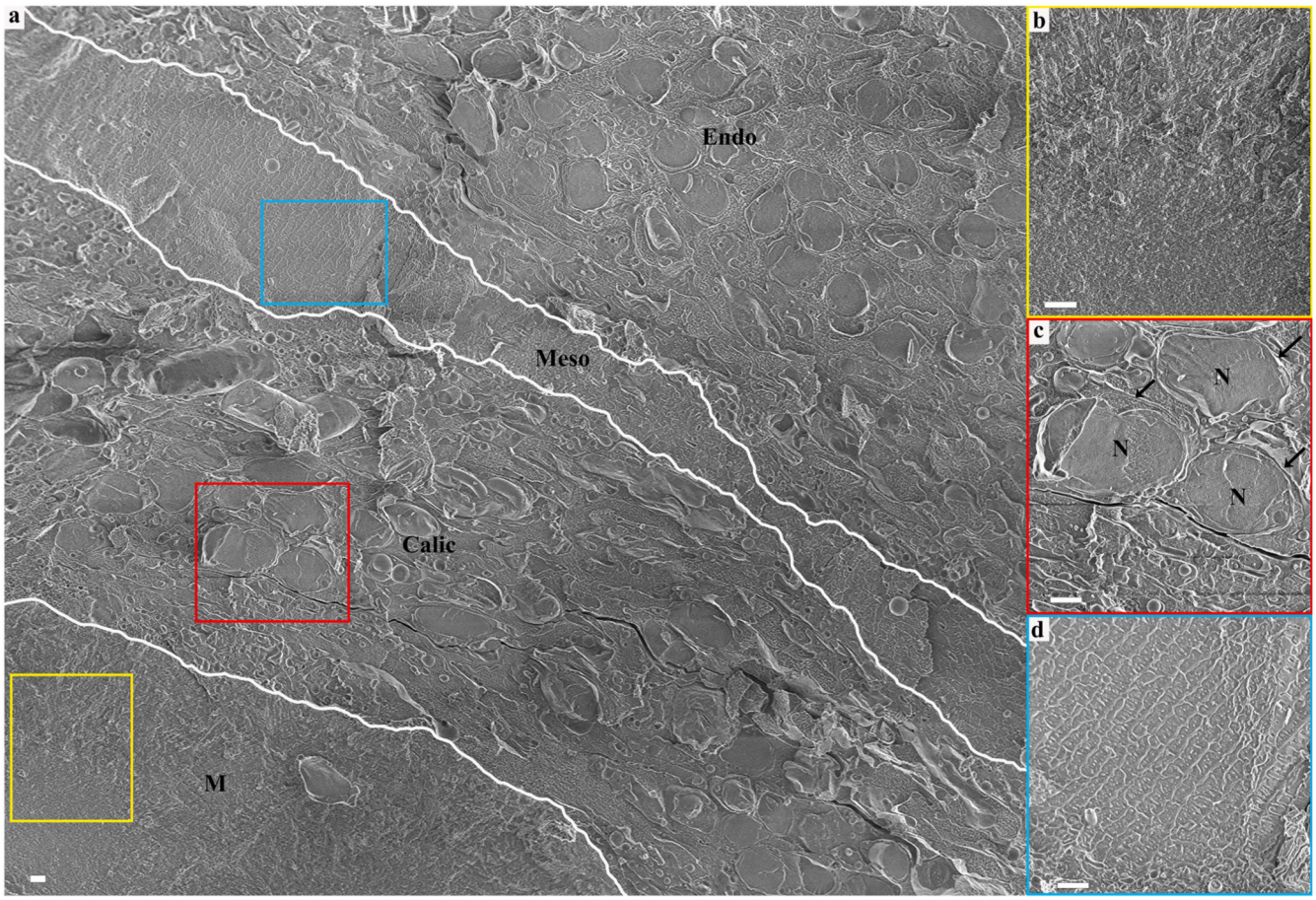

Fig. 2. A cryo-SEM micrograph of aboral body layers observed in a high–pressure frozen, freeze-fractured primary polyp.

(a) An overview image showing aboral body layers depicted by white separating lines including the mineral, **M**, (Yellow rectangle is magnified in (b)), the calicoblastic cell layer, **Calic**, (Red rectangle is magnified in (c)), the noncellular mesoglea, **Meso**, (Light blue rectangle is magnified in (d)) and the endoderm (**Endo**). **N**-Nucleus. All scale bars are 1 μm.

Europe PMC Funders Author Manuscripts

Europe PMC Funders Author Manuscripts

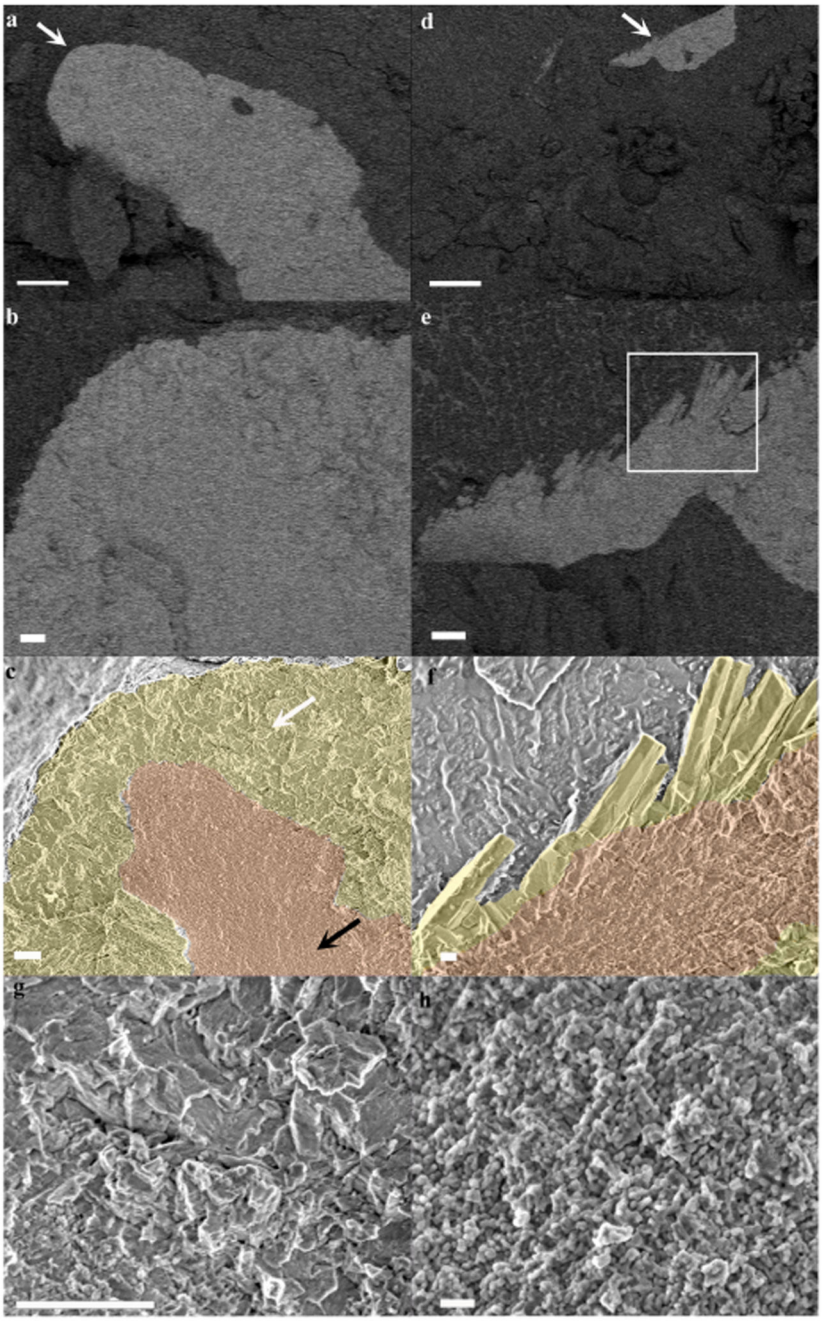

Fig. 3. Cryo-SEM micrographs of mature and forming septa in a primary polyp.

(a) A mature septum imaged in EsB mode. Mineral appears brighter than its surrounding tissue. (b) Magnification of the area pointed with white arrow in (a). (c) The same areas as in (b) imaged in SE mode with CoC and elongated microcrystals highlighted by false coloring. (d) A newly formed septum imaged in EsB mode. (e) Magnification of the area pointed with white arrow in (d). (f) SE mode image of the area marked with white rectangle in (e) with CoC and elongated microcrystals highlighted by false coloring. (g) Higher magnification of micron sized crystals' fracture surface pointed with white arrow in (c). (h) Higher

magnification of CoC nano-spheres texture pointed with black arrow in (c). Orange-CoC. Yellow-elongated microcrystals. Scale bars are (a)-and (d)-10 μm, (b), (c), (e) and (g)-1 μm, (f)-200 nm, (h)-100 nm.

Europe PMC Funders Author Manuscripts

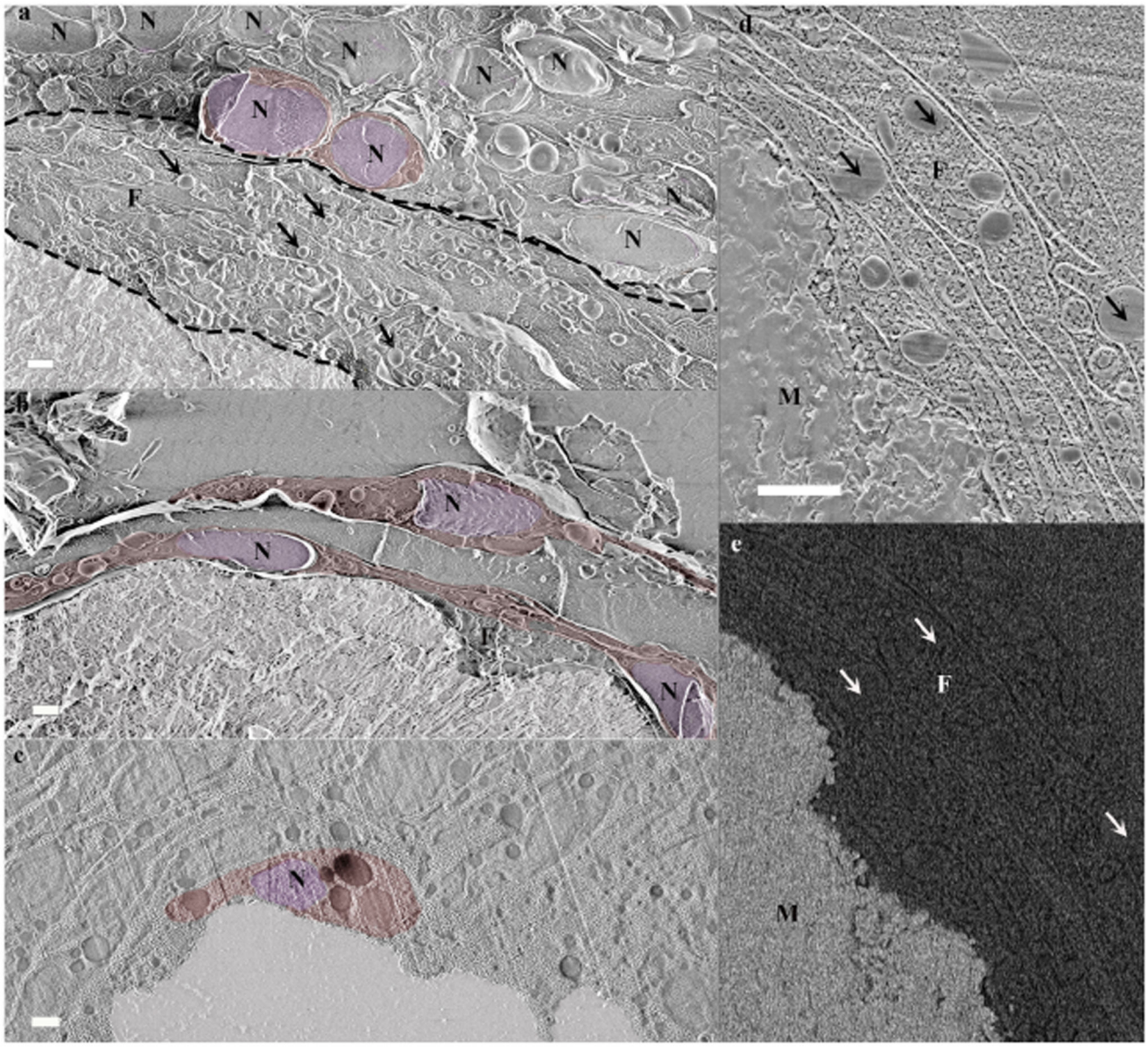

Fig. 4. Calicoblastic cell morphologies observed in freeze-fractured (a-b) and cryo-planed (c-e) primary polyps using cryo-SEM.

(a) Calicoblastic cell layer (imaged locus is the same as in Fig. 2c with the septum mineral and two representative calicoblastic cells highlighted by false coloring. A filopodia network found between the calicoblastic cell bodies and the septum is denoted between two dashed black lines. Four representative vesicles contained within the filopodia network are denoted with black arrows. (b) Three elongated calicoblastic cells found in close proximity with the mineral. (c) A cup shaped calicoblastic cell attached to the mineral surface. (d) High magnification of filopodia found in close proximity with the mineral (SE mode). (e) The same field of view as in (d) imaged in EsB mode. False coloring is used to highlight: cell nucleolus (pseudo-purple), cell body (pseudo-red), septum mineral (pseudo-white). Scale bars are 1 μm. **N**-nucleus, **F**-filopodia, **M**-mineral.

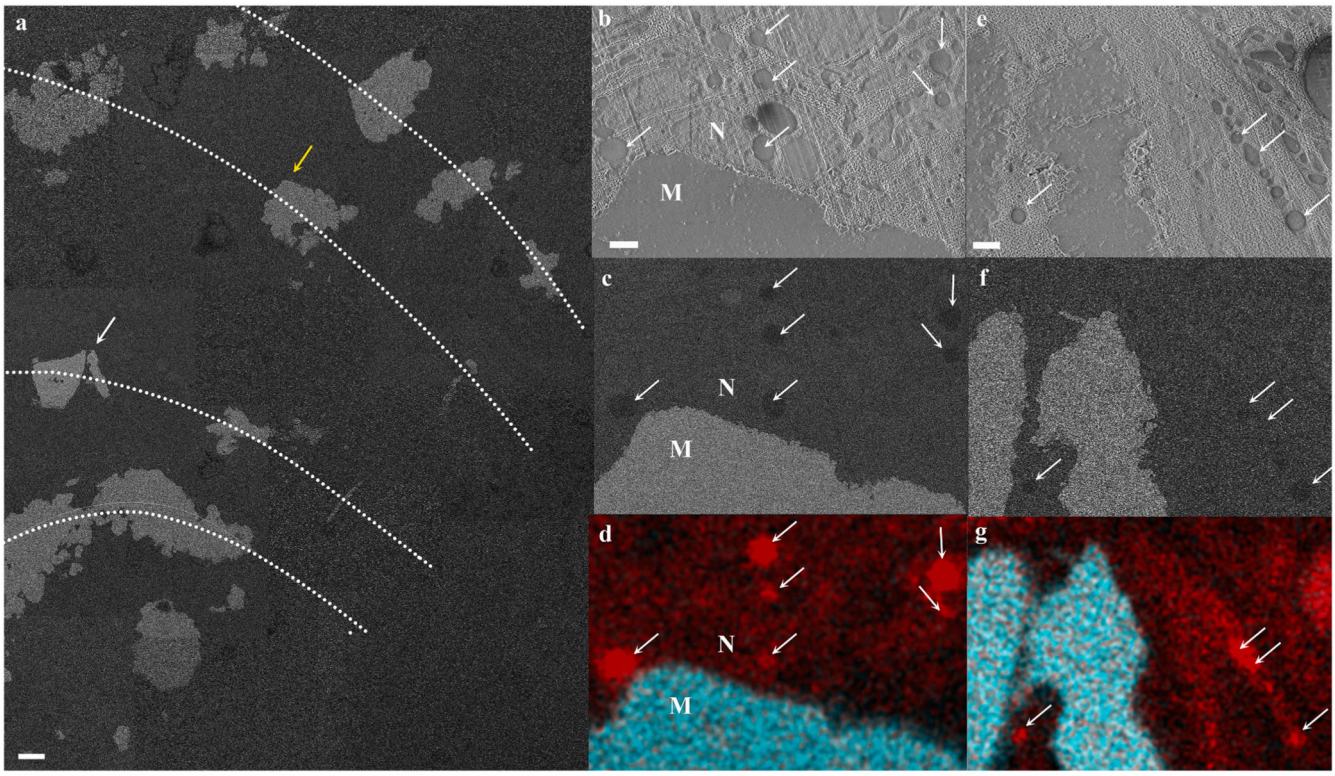

Fig. 5. Cryo-SEM/EDS analysis of calicoblastic cells in a cryo-planed primary polyp.

(a) An overview collage image composed of several high magnification cryo-SEM (EsB mode) micrographs stitched together, showing the cryo-planed surface along several septa (dotted lines represent septa long axes) in a primary polyp. The mineral surfaces of the planed septa appear white, and the coral soft tissues appear grey. (b-d) High magnification of locus pointed with a yellow arrow in (a) (same area as in Fig. 4c showing a cup-shaped calicoblast attached to the mineral imaged in SE, EsB and EDS map, respectively. (e-g) High magnification of locus pointed with a white arrow in (a) showing filopodia in close proximity with the mineral imaged in SE, EsB, and EDS maps, respectively. Carbon-rich vesicles are pointed with white arrows in (b)-(g). EDS maps show carbon (red) and calcium (turquoise) distributions. **M**-mineral, **N**-nucleus. Scale bars: (a)-10 μm, (b-g)-1 μm.

Europe PMC Funders Author Manuscripts

Europe PMC Funders Author Manuscripts

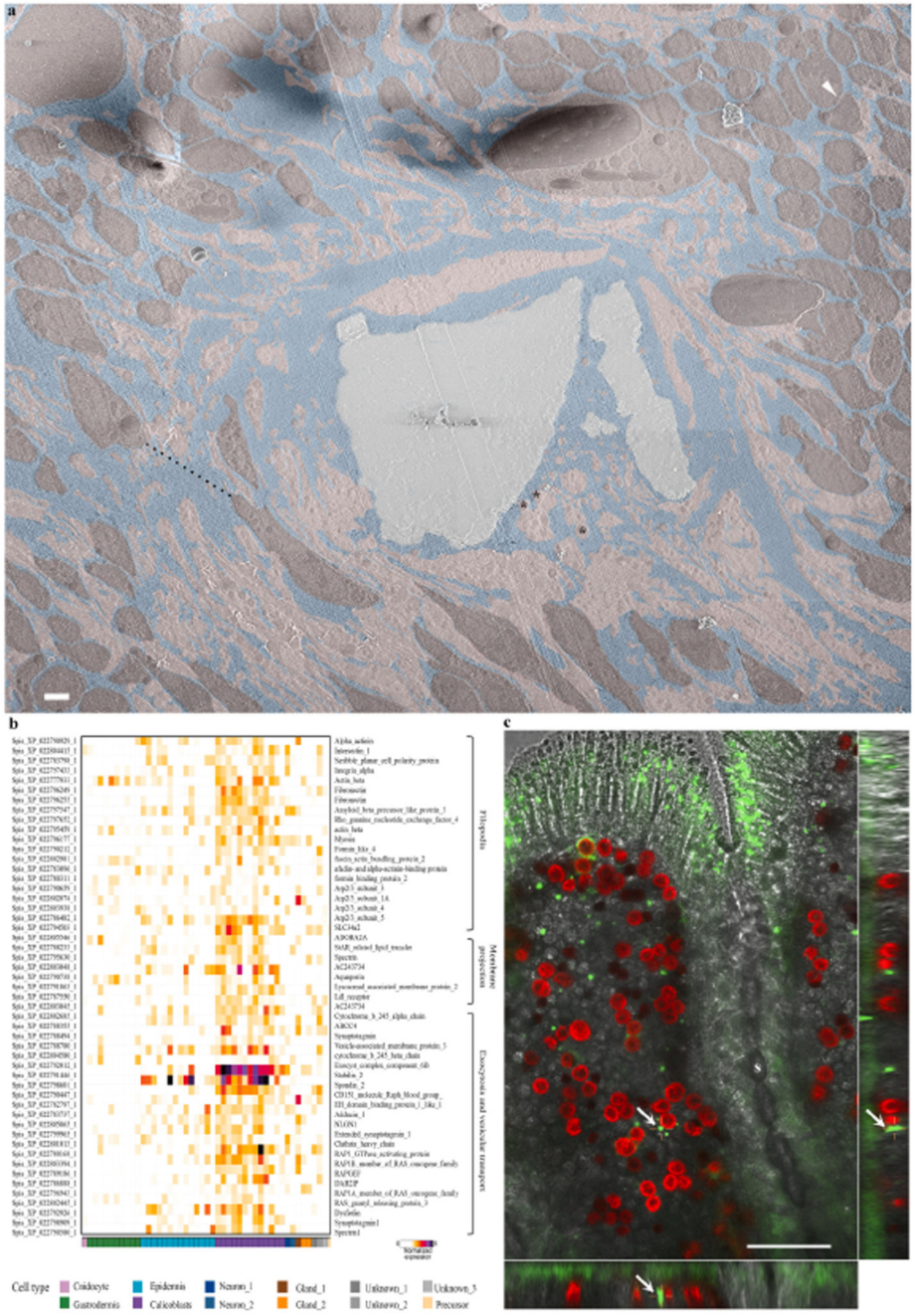

Fig. 6. The paracellular space in primary polyps.

(a) An overview image stitched from several high magnification cryo-SEM micrographs of the calicoblastic tissue around a septum in a cryo-planed primary polyp (same area as pointed with a white arrow in Fig. 5a. Tightly packed calicoblastic cells with a paracellular spacing of 30 nm are pointed with a white arrowhead (top right corner). Dispersed cell packing with a paracellular space of 8.4 μm is denoted with a black dashed line. Calicoblastic cell bodies are highlighted with pseudo–burgundy, filopodia in pseudo–pink, ECM in pseudo–blue, and the mineral in pseudo–grey. Three representative vesicles

contained within the filopodia network are marked with black asterisks. Scale bar is 2 μm. (b) Gene expression heatmap for selected genes involved in filopodia structure and function, membrane projections, exocytosis, and vesicular transport across all cell types of *S. pistillata* primary polyp (all selected genes are highly expressed in the calicoblasts cells -purple). (c) In-vivo confocal laser scanning fluorescence image of the coral tissue around a septum (s) in a primary polyp labeled with green-fluorescent beads of 1 μm diameter. Green-fluorescent beads, red-symbionts auto-fluorescence, grey scale-transmitted laser scanning image. The center large panel is one horizontal (xy) plane taken 16 μm above the glass, roughly in the middle of the z-stack data set covering the entire sample thickness (30 μm). The right and bottom panels are two side views of the z-stack data set (i.e. xz, and yz) showing fluorescent beads incorporated inside the coral tissue. One representative green-fluorescent bead is depicted with a white arrow in all three panels.

Europe PMC Funders Author Manuscripts

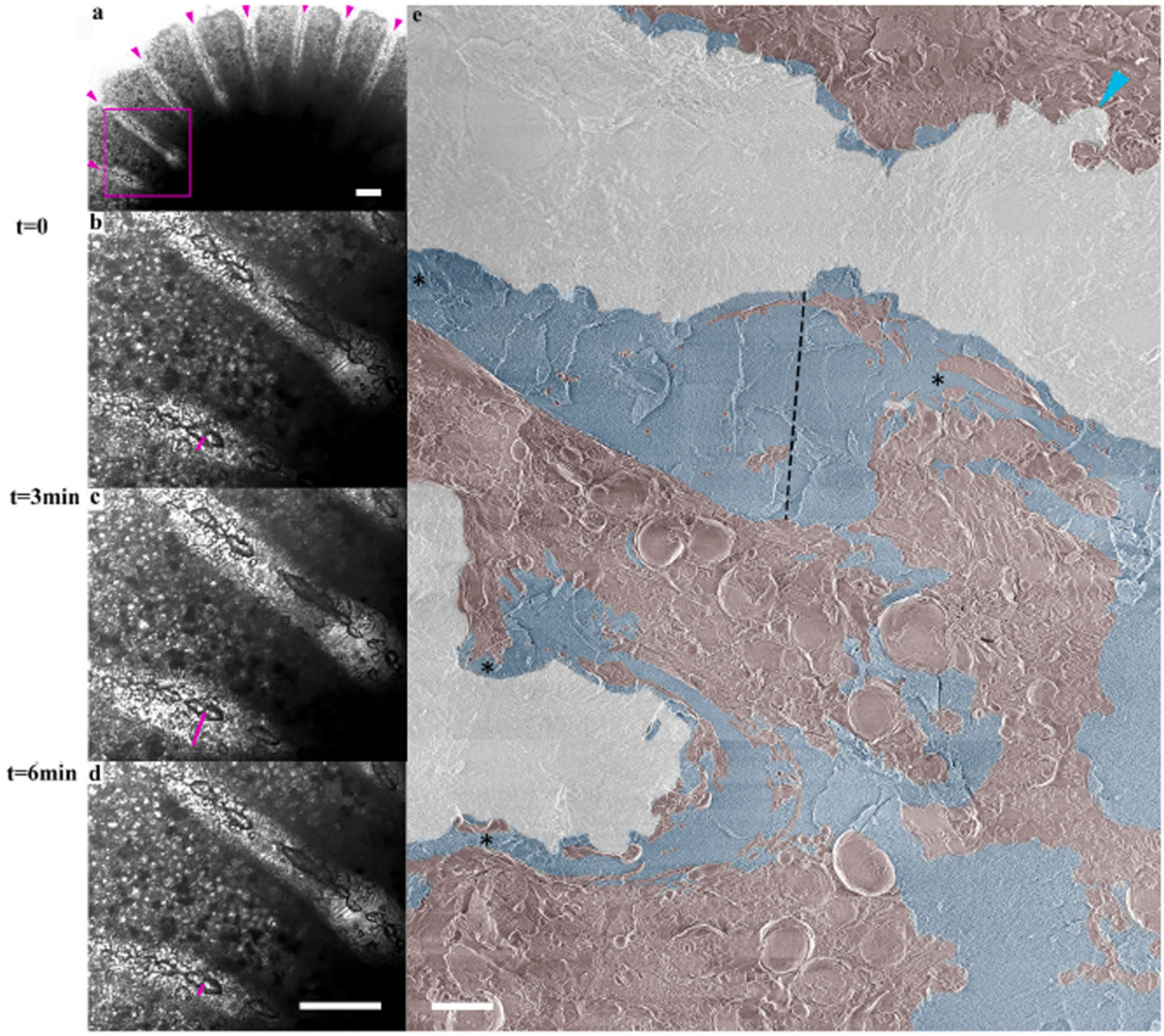

Fig. 7. ECM thickness variation along primary polyp septa.

a) Transmitted laser scanning in-vivo microscopy image of a primary polyp with forming septa denoted with magenta arrowheads recorded at t = 0. (b)-(d) Higher magnification of the area marked with a magenta square in (a) recorded at t = 0, t = 3 min, and t = 6 min respectively (see also movie S1). The thickness of the ECM on the bottom side of one septum is marked with a magenta line and equals 27 μm, 43 μm, and 18 μm, respectively. (e) A collage overview image stitched from high-resolution cryo-SEM micrographs of a septum in a freeze-fractured primary polyp. Mineral surface-pseudo white, ECM-pseudo blue, coral tissue (including cell bodies and filopodia)-pseudo-burgundy. ECM layer thickness in an 'ECM pocket' is depicted by a dotted black line and equals 38 μm. ECM layer narrowing is pointed with asterisks. Coral tissue closely attached to the mineral surface is pointed with turquoise arrowhead (upper right corner). Scale bars: (a-d): 100 μm, (e): 10 μm.

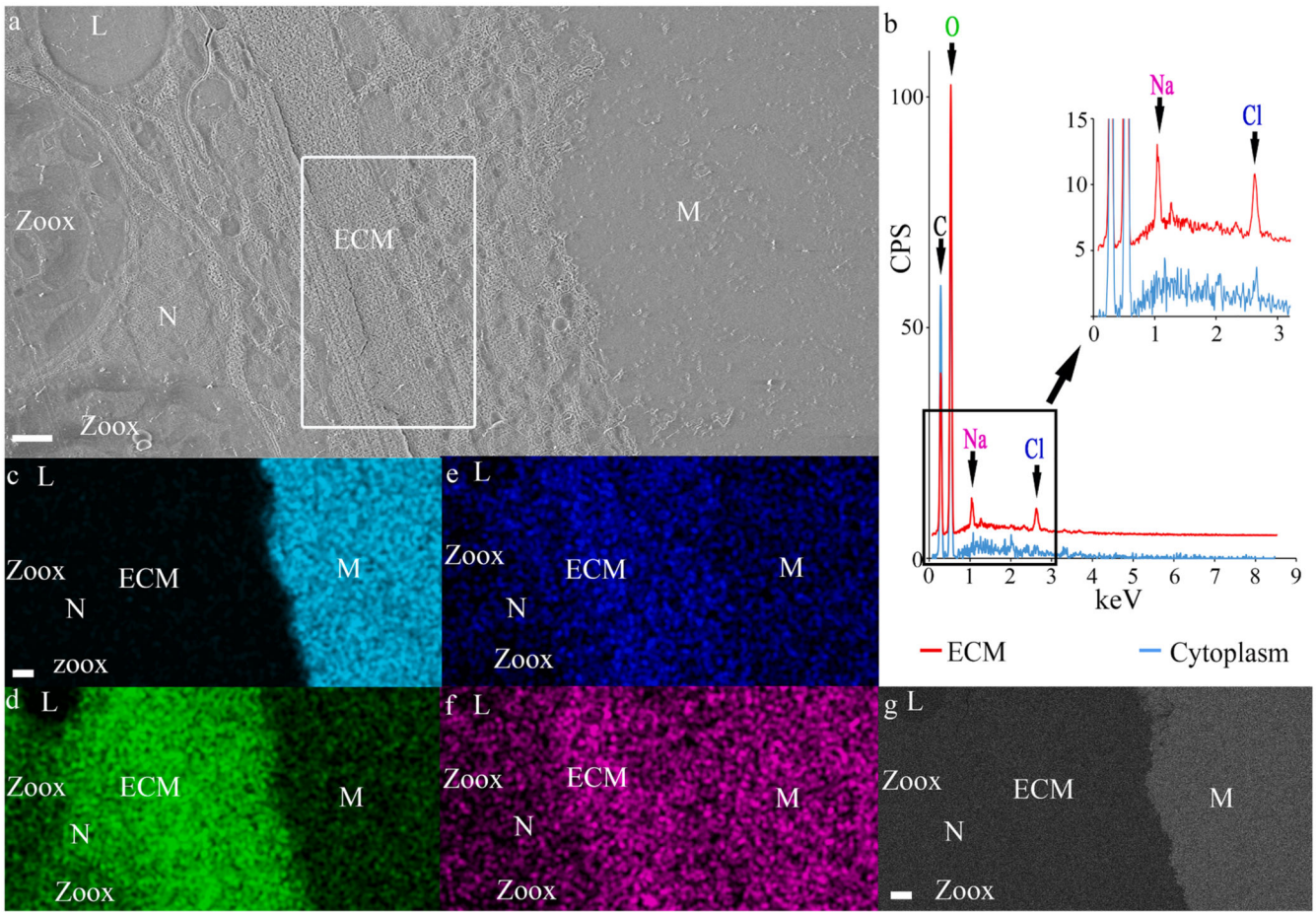

Fig. 8. Cryo-SEM/EDS analysis of the ECM

(a) SE mode micrograph of the tissue–mineral interface. (b) Cryo-EDS spectra of the ECM (measured area is marked with a white rectangle in (a)) and of the cytoplasm in a calicoblastic cell. Identified elements are labeled in the graph. (c)-(f) Cryo-EDS elemental distribution maps of the same area as in image (a): of the elements: Calcium (Cyan), oxygen (Green), chlorine (Blue), and sodium (Magenta). (g) Cryo-EsB micrograph of the same area as in (a)-(f). All scale bars are 1 μm. M = Mineral, N = Nucleolus, Zoox = algal symbiont, L = Lipid body. CSP = counts per second.

Europe PMC Funders Author Manuscripts